Journal of Fluids and Structures 91 (2019) 102732

Contents lists available at ScienceDirect

Journal of Fluids and Structures

journal homepage: www.elsevier.com/locate/jfs

Analysis of array spacing on tidal stream turbine farm performance using Large-Eddy Simulation

Pablo Ouro [a,*], Luis Ramírez [b], Magnus Harrold [c]

[a] Hydro-environmental Research Centre, School of Engineering, Cardiff University, The Parade CF24 3AA, Cardiff, United Kingdom
[b] Group of Numerical Methods in Engineering, University of A Coruña, Campus de Elviña, 15071, A Coruña, Spain
[c] College of Engineering, Mathematics and Physical Sciences, University of Exeter, TR10 9FE Penryn, United Kingdom

ARTICLE INFO

Article history:
Received 15 February 2019
Received in revised form 1 August 2019
Accepted 2 September 2019
Available online 12 September 2019

Keywords:
Horizontal axis tidal turbines
Wake-device interaction
Arrays
Wake recovery
Fatigue
Tidal energy
LES
ALM

ABSTRACT

Design of efficient tidal arrays relies on the adopted spacing between turbines and their mutual interplay. Turbines affected by wake shadowing operate in harsher flow conditions, such as higher turbulence levels or lower incident velocity, which leads to reduced performance and larger extreme and fatigue loading. To extend the knowledge about turbine-to-turbine interplay in tidal arrays, high-fidelity numerical simulations using a Large-Eddy Simulation-Actuator Line Method (LES-ALM) are carried out to quantify the impact of row spacing. The developed Digital Offshore FArm Simulator (DOFAS) validates well with experimental data in terms of flow statistics and hydrodynamic coefficients, which demonstrate its adequacy to resolve the complex fluid-turbines interaction. In the cases with spacing of four and eight diameters between the rows, the lack of wake recovery has a detrimental effect on back-row turbines whose efficiency dramatically drops compared to those in the front-row. The LES-ALM captured the low-frequency wake meandering phenomenon responsible for uneven periodic loading on back-row turbines. The devices placed in the front-row suffer the largest thrust loads, blade-root bending moments and support structure moments, whilst the outermost back-row turbines experience the largest tower yaw moments due to their simultaneous exposure to low-momentum turbulent wakes and high-velocity free-stream flow. Finally, damage equivalent loads estimated by the LES-ALM are maximum for the front-row turbines except the tower yaw moment which is maximum on the outermost back-row turbines.

1. Introduction

To date, the offshore renewable energy sector at commercial scale is predominately dedicated to harness energy from wind with farms comprising dozens of turbines found around the globe (Porté-Agel et al., 2013). The dynamics of wind at offshore sites and its interaction with the operating turbines has been well studied (Yang et al., 2015b; Sanz Rodrigo et al., 2017) which allowed to identify and quantify key phenomena such as the internal boundary layer developed from the interaction of the operating turbines with the oncoming wind (Cal et al., 2010), or the turbine-to-turbine interaction due to wake meandering responsible for long-term fatigue loadings (Churchfield et al., 2012).

Tidal stream turbines are at a much earlier stage of maturity with a handful farms deployed and providing electricity to the grid (Magagna and Uihlein, 2015). There is an obvious advantage of tidal energy over its wind counterpart: its

* Corresponding author.
E-mail address: OuroP@cardiff.ac.uk (P. Ouro).

https://doi.org/10.1016/j.jfluidstructs.2019.102732

predictability (Ahmadian and Falconer, 2012). Unlike the stochastic wind resources, the direction and magnitude of tidal currents can be predicted with a higher degree of accuracy (Ramos et al., 2014). Hence, it is possible to predict the energy that can be harnessed for long periods of time from a given sea site and, ultimately, optimise the arrays of turbines (Funke et al., 2015; Vennell et al., 2015).

A commonality between wind and tidal farms' dynamics is the wake shadowing, i.e. wake-turbine interactions between devices in different rows, which has detrimental effects on the performance and loadings (Porté-Agel et al., 2013; Churchfield et al., 2012). Rev Horns wind farm is an example in which such phenomenon signified a notable detriment in the whole farm performance due to a reduced momentum recovery after the first row of turbines (Mehta et al., 2014). The turbines in downstream rows experienced a reduction in their energy generation capabilities being up to a 40% lower than the turbines in the first row. Such experience gained from wind energy should be now taken into consideration in tidal turbine array design.

Early studies in the characterisation of the hydrodynamics in tidal turbine farms adopted analytical models to describe the wake velocity profiles as a result of local and global blockage (Garrett and Cummins, 2007), free-surface effects (Whelan et al., 2009) or comparison between centred and staggered arrays (Draper and Nishino, 2014). Despite the lack of modelling instantaneous flow effects, e.g. turbulence, these theoretical models provided important findings that were then supported by experimental campaigns and high-fidelity computational models. For instance, Olczak et al. (2016) and Draper and Nishino (2014) found that turbines deployed in staggered arrangement provided a greater performance than when placed with a centred configuration. Draper and Nishino (2014) also argued the array layout that would maximise extraction of kinetic energy from the tidal resource would be having all turbines across the same cross-stream location, i.e. avoiding wake-turbine interactions. Despite the latter being valid from an analytical point of view, real-life projects have a limited decommission area in which many turbines need to be placed in subsequent rows to maximise energy generation so these can be economically viable.

Experimental testing of arrays of tidal turbines are limited due to the need for facilities that allow to place multiple devices and control flow conditions. Mycek et al. (2014a) studied two in-line turbines under different separation distances and environmental conditions, finding that under highly-turbulent conditions the downstream turbine is less affected by the upstream one due to a faster wake recovery. Stallard et al. (2013) observed that increasing the hub-to-hub separation between turbines in the same row, the downstream distance at which individual wakes merge increases. Chawdhary et al. (2017) performed experimental tests and high-fidelity simulations of three turbines sharing a triangular-shaped support structure and observed that the overall power output of these devices is higher in such close arrangement than if placed individually. Musa et al. (2018) investigated the effect of a scaled array of hydro-kinetic turbines on the morpho-dynamics of rivers and found, despite these devices' wakes are highly turbulent, they had minimal disruption in the natural sediment transport processes.

Reproducing the complex environmental conditions as those found at offshore sites is extremely difficult in experimental hydraulic flumes, and thus computational models arise as a powerful tool to be used complementary to experiments (Nash and Phoenix, 2017). Accurate and computationally affordable numerical models capable of resolving the flow unsteadiness and turbine-to-turbine interactions in tidal arrays are limited. The development of such models is of great interest to both academia and industry as they would provide invaluable flow information to better design tidal arrays, including in the simulations features such as ambient turbulence intensity and length scales, vertical distribution of velocities, bathymetry effects and waves. Hence, these numerical models need to accurately capture turbulence-related phenomena which implies resolving, at least, the most energetic flow structures. Under such demand, depth-averaged or Reynolds Averaged Navier–Stokes (RANS) models can provide a reasonably accurate predictions of mean wake deficit (Olczak et al., 2016; Masters et al., 2015; Apsley et al., 2018; Abolghasemi et al., 2016), but are unable to resolve any flow unsteadiness with the modelled velocity fluctuations notably differing depending on the turbulence model used (Shives and Crawford, 2016). Alternatively, eddy-resolving approaches, such as Large-Eddy Simulation (LES), can capture unsteady flow properties (Stoesser, 2014) as well as time-dependent structural loadings on tidal turbines (Afgan et al., 2013).

LES has been proven to be an adequate high-accuracy technique to resolve the complex flow around tidal turbines capturing phenomena such as the transient wake behaviour of the wakes (Kang et al., 2014; Foti et al., 2016) or impact of environmental turbulence (Ouro and Stoesser, 2019). Afgan et al. (2013) demonstrated the superiority of LES over RANS in the simulation of a single turbine with the latter model failing in predicting tip vortices or regions of high turbulence immediately behind the turbine. Churchfield et al. (2013) performed the LES of an array of tidal turbines and quantified that back-row turbines largely suffer from the wake of the upstream turbines when in in-line arrangement on the contrary to staggered configurations. Kang et al. (2014) simulated a single tidal turbine with different Lagrangian techniques to represent the device and found that the Actuator Line Model (ALM) provided similar accuracy in the mean wake prediction and captured main flow dynamics, i.e. tip vortices or hub wake, compared to geometry resolved simulations using the immersed boundary method. Baba-Ahmadi and Dong (2017) further confirmed the performance of the coupling of LES-ALM to accurately predict the flow statistics in the wake of a single tidal turbine.

Here a LES-ALM is implemented in the in-house code Hydro3D (Ouro et al., 2019a) and is used to analyse the flow developed in three arrays of turbines investigating the wake hydrodynamics and structural loads in terms of maximum and equivalent fatigue loads. The paper is structured as follows: the complexity of the hydrodynamics in tidal turbine arrays is described in Section 2. Section 3 presents the LES method adopted to resolve the fluid flow and the Actuator

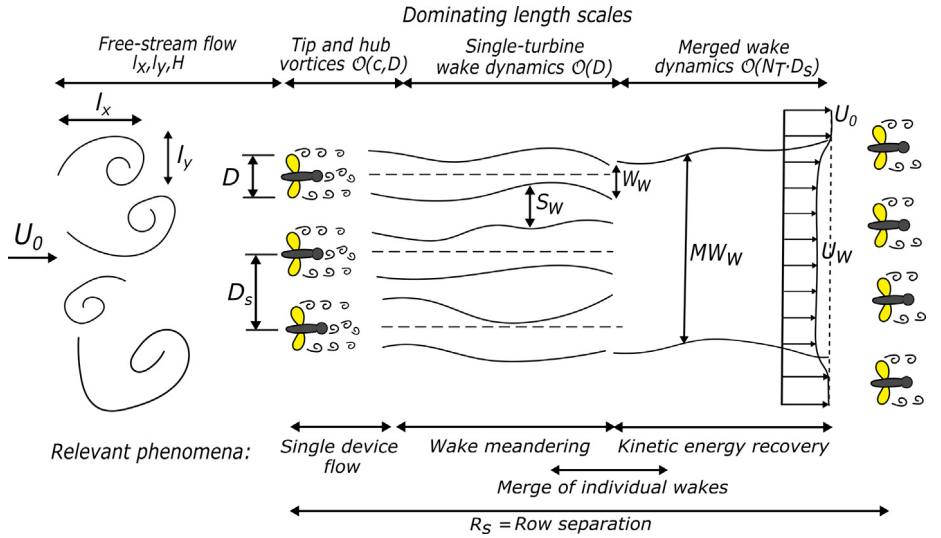

Fig. 1. Schematic of the hydrodynamics of an array of tidal turbines.

Line Model (ALM) to represent the turbines, which yields the proposed Digital Offshore FArm Simulator (DOFAS). The validation of the LES-ALM model with experimental data is presented in Section 5, followed by the analysis of the wake flow statistics, hydrodynamic coefficients, structural loadings, and equivalent fatigue loads. In Section 6, the conclusions from this study are drawn.

2. Problem description

An overview of the main flow phenomena developed in arrays of tidal stream turbines is depicted in Fig. 1, with the turbines deployed in several rows in a staggered fashion as it is accepted to be more efficient than centred layouts. In a tidal farm, turbulence intensity and, more importantly, turbulence length scales of the free-stream flow directly influence the wake recovery after the first rows (Mycek et al., 2014b; Ouro et al., 2017). In the turbines' wakes, three key phenomena can be highlighted: tip vortices generated as the shear introduced by the blades' tips, a low-velocity hub wake, and wake meandering in the far-wake (Kang et al., 2014; Foti et al., 2016). Tip vortices are usually of relatively small size and can lose coherence few diameters downstream of the turbine whilst the low-frequency meandering of the wake can persist for many diameters downstream. Additionally, considering a scenario comprising multiple N_T turbines, each individual wake extends a given transverse distance width, W_W, which can merge with those induced by adjacent turbines depending on their inter-turbine or lateral separation, D_s, i.e. closer hub-to-hub spacing leads to faster merging (Stallard et al., 2013). These individual wakes are separated a distance S_W and eventually converge to a single Merged Wake, MW, whose lateral extension, MW_W, is in the order of $\mathcal{O} \sim (N_T \cdot D_s)$.

Three main regions in the wake of turbines at any row can be distinguished: near-wake, in which the length scales of the dominant turbulent structures introduced by every device are in the order of the blade chord (c) and turbine diameter (D); mid-wake, where individual hub wakes and wake meandering dominate; and far-wake, characterised by a faster rate of kinetic energy recovery (Ouro and Stoesser, 2019). Understanding and characterising these different wake regions and dominant flow phenomena, aid to determine the appropriate distances within the mid- and far-wakes to deploy secondary rows of tidal turbines with the goal of minimising detrimental wake-turbine interaction effects (Myers and Bahaj, 2012).

3. Numerical framework

3.1. Large-eddy simulation solver

In the present simulation of multiple tidal stream turbines are carried out using the in-house large-eddy simulation code Hydro3D (Ouro et al., 2018). This open-source code has been previously validated with success in numerous engineering applications (Stoesser, 2010; Bomminayuni and Stoesser, 2011; Kara et al., 2015; McSherry et al., 2018) and features an efficient fluid solver fully parallelised with Message Passing Interface (MPI) together with a Local Mesh Refinement (LMR) algorithm (Cevheri et al., 2016). Hydro3D features a refined immersed boundary method (IBM) (Ouro and Stoesser, 2017) that has been recently parallelised using a novel hybrid MPI/OpenMP scheme embedded within a master-scattering-gathering strategy that efficiently deals with moving bodies (Ouro et al., 2019a). Ouro and Stoesser (2019) and Ouro et al. (2017) adapted the IBM for the large-eddy simulation of geometry-resolved horizontal axis

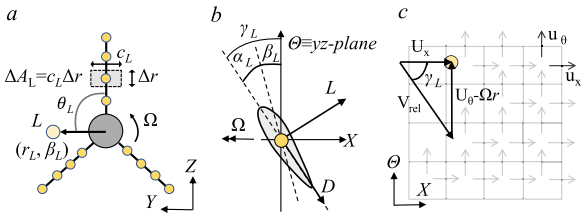

Fig. 2. Representation of a tidal turbine rotor using the actuator line method. (a) Three-bladed rotor, (b) 2D hydrofoil, and (c) relative velocity obtained from the interpolated fluid velocities.

tidal turbines which allowed the identification of the most relevant large-scale structures in the flow as well as the quantification of the effect of uneven bathymetry on the wake recovery.

Hydro3D solves the governing equations in LES that are the spatially-filtered three-dimensional Navier–Stokes equations for incompressible viscous flow,

$$\frac{\partial u_i}{\partial x_i} = 0 \tag{1}$$

$$\frac{\partial u_i}{\partial t} + u_j\left(\frac{\partial u_i}{\partial x_j} - \frac{\partial u_j}{\partial x_i}\right) = -\frac{1}{\rho}\frac{\partial p}{\partial x_i} + \nu\frac{\partial^2 u_i}{\partial x_j^2} - \frac{\partial \tau_{ij}}{\partial x_j} + \frac{f_i}{\rho} \tag{2}$$

where u_i is the vector of filtered velocities, x_i is the vector of the spatial coordinates, p is the filtered relative pressure, ν is the kinematic viscosity, ρ is the fluid's density, f_i is a source term, and the Sub-Grid Stress (SGS) tensor τ_{ij} is computed using WALE model of Nicoud and Ducros (1999) as it has been proven to adapt well when moving bodies are simulated (Ouro and Stoesser, 2017). Rectangular Cartesian grids are used to discretise the computational domain with staggered storage of velocities and second-order central differences are adopted to approximate flow derivatives. A fractional-step method with a third order Runge–Kutta method is used to advance the simulation in time (Chorin, 1968).

3.2. Actuator line model

The Actuator Line Model (ALM) is implemented in the LES-code Hydro3D (Ouro et al., 2019b) enhancing its capabilities to model multiple turbines at a reasonable computational expense, which enables it to become a Digital OFfshore FArm Simulator (DOFAS). The ALM discretises each turbine blade into a number of sections N_l depending on the blade's length L_b and computational grid resolution in the vertical direction, i.e. $N_l = L_b/\Delta z$. Fig. 2a depicts how a tidal stream turbine rotor is discretised by means of the ALM into a finite number of sections, each one represented by a marker L whose area ΔA_L results from the section vertical length $\Delta r = \Delta z$ and its chord length c_L, i.e. $\Delta A_L = \Delta r c_L$.

The set of solid markers that comprise the geometry of the blades moves according to the rotational speed of the turbine, Ω, along the computational mesh and interpolation functions are responsible for transferring velocities and forces between Lagrangian and Eulerian frameworks. Note that from hereinafter lower-case and upper-case variables refer to fluid and solid frameworks, respectively. At every time step, the fluid velocities $\boldsymbol{u}(\mathbf{x}, t) = (u, v, w)^T$ from the closest n_e neighbours to each marker comprising the turbine's rotor are interpolated to the Lagrangian grid to obtain the Lagrangian velocity $\boldsymbol{U}_L = (U_x, U_y, U_z)^T$. This is performed by means of delta functions, δ, specifically the ϕ^4 function from Yang et al. (2009) that uses 64 neighbours in 3D with a kernel support width of $4\Delta x_i$, as follows,

$$\boldsymbol{U}_L(\boldsymbol{X}_L, t) = \sum_{i=1}^{n_e} \boldsymbol{u}(\boldsymbol{x}_i, t) \cdot \delta\left(\frac{\boldsymbol{x}_i - \boldsymbol{X}_L}{\Delta \boldsymbol{x}_i}\right) \cdot \Delta \boldsymbol{x}_i^3 \tag{3}$$

As indicated in Fig. 2b, the relative velocity vector, V_{rel}, at each marker is $(U_x, U_\theta - \Omega r)^T$, with U_x being the x-direction interpolated velocity component and U_θ the tangential interpolated velocity component in the yz-plane of rotation determined as $U_y \cdot sin(\theta_L) + U_z \cdot cos(\theta_L)$, where θ_L is the angle rotated by the marker. As presented in Fig. 2c, the incidence angle attained by each marker, γ_L, is determined as,

$$\gamma_L = \text{atan}\left(\frac{U_x}{U_\theta - \Omega r}\right) \tag{4}$$

The effective angle of attack, α, results from the difference between the incidence angle and the section's fixed pitch angle β, i.e. $\alpha = \gamma - \beta$. The next step is to compute Lift (L) and Drag (D) forces as,

$$(L, D) = \frac{1}{2}\rho |V_{rel}|^2 \cdot (C_L, C_D) \cdot \Delta A_L \cdot F1 \tag{5}$$

where $|V_{rel}| = (U_x^2 + (U_\theta - \Omega r)^2)^{0.5}$ is the relative velocity module, C_L and C_D are the tabulated hydrodynamic characteristics for each marker and $F1$ is a Prandtl-type tip-loss correction term as proposed in Shen et al. (2005). In the analysis of tidal

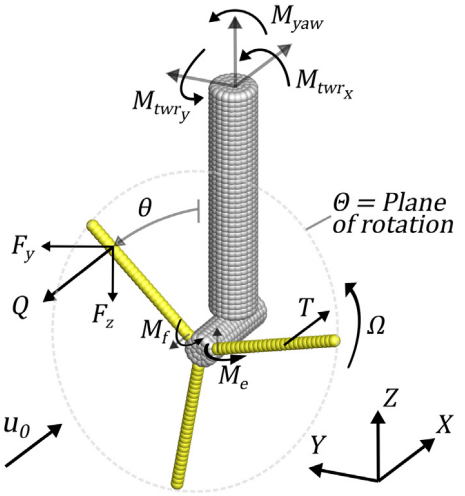

Fig. 3. Representation of the relevant structural moments calculated in a tidal turbine rotor using the actuator line method.

turbines it is of interest to obtain the forces in the x-direction, namely thrust T_L, and the tangential force, F_θ, which is responsible for the generation of torque as $Q_L = F_{\theta_L} R_L$. Hence, lift and drag forces are projected onto these planes of interest considering the local effective angle of attack α_L as,

$$T_L = D \cdot sin(\alpha_L) + L \cdot cos(\alpha_L) \tag{6}$$

$$Q_L = D \cdot cos(\alpha_L) - L \cdot sin(\alpha_L) \tag{7}$$

The latter forces are in the inertial reference system of the turbine (X, Θ) and are projected onto the Cartesian reference framework $(\boldsymbol{x})$ using the rotated angle of each marker θ_L as,

$$F_{y_L} = Q_L \cdot cos(\theta_L) \tag{8}$$

$$F_{z_L} = -Q_L \cdot sin(\theta_L) \tag{9}$$

The resulting force vector $\boldsymbol{F}_L(\boldsymbol{X}_L) = (T_L, F_{y_L}, F_{z_L})^T$ are projected onto the Eulerian fluid cells to obtain the forcing term f present in the r.h.s. of the momentum equation (Eq. (2)), which is responsible for correcting the fluid velocities as a result of the turbine action. During this backwards interpolation, the delta functions computed during the forwards interpolation are adopted with the number of neighbours N_L equal to n_e (Ouro et al., 2019a), and calculated as,

$$\boldsymbol{f}_i(\boldsymbol{x}_i, t) = \sum_{L=1}^{N_L} \boldsymbol{F}_L(\boldsymbol{X}_L, t)/\Delta A_L \cdot \delta\left(\frac{\boldsymbol{X}_L - \boldsymbol{x}_i}{\Delta \boldsymbol{x}_i}\right) \cdot \Delta \boldsymbol{x}_i^3 \tag{10}$$

3.3. Support structure modelling

In DOFAS, the turbine hubs and vertical support structures are modelled using the Immersed Boundary Method (IBM) which has been successfully validated in previous works (Ouro et al., 2017; Ouro and Stoesser, 2017). This IBM is based on the direct forcing method proposed in Uhlmann (2005) that is based on discretising a solid body into a set of individual markers at whose location a no-slip condition is enforced to represent its effect onto the fluid. The methodology adopted in the IBM and ALM share some commonality as they use the same interpolation method, i.e. discrete interpolation functions, to exchange information between solid and fluid frameworks. However, the ALM forces are computed from predetermined hydrodynamic properties, such as C_L and C_D, whilst the IBM resolves the actual hydrodynamics of the turbine enforcing a no-slip condition (Uhlmann, 2005) or adopting wall functions (Kang et al., 2012).

The main structural forces acting on a single tidal turbine are presented in Fig. 3. Those acting on the rotor are: thrust force (T), tangential force (Q), edge-wise (M_e) and flap-wise (M_f) bending moments, while yaw moment (M_{yaw}) and x-(M_{twr_x}) and y-moments (M_{twr_y}) act on the support structure and are also of interest (Churchfield et al., 2012).

Thrust and power coefficients are used as reference in the fluid–structure interaction and are defined as,

$$C_x = \frac{T}{\frac{1}{2}\rho A u_0^2} \tag{11}$$

$$C_p = \frac{Q\Omega}{\frac{1}{2}\rho A u_0^3} \tag{12}$$

where A denotes the rotor swept area $A = \pi R^2$ and u_0 is the free-stream velocity.

4. Test cases and computational setup

The experimental work performed from Stallard and colleagues (Olczak et al., 2016; Stallard et al., 2013, 2015) is herein reproduced with DOFAS. The hydraulic flume used during experiments was 5 m wide with a water depth H equal to 0.45 m and a total longitudinal extension of 12.5 m. Stallard et al. (2015) collected flow statistics throughout the water depth at the turbine position without the device being placed. The obtained vertical distribution of streamwise velocities follows a logarithmic distribution, Eq. (13), and yields a depth-averaged velocity of $u_0 = 0.47$ m/s.

$$\frac{u(z)}{u^*} = \frac{1}{\kappa}\ln\left(\frac{u^* z}{\nu}\right) + C \tag{13}$$

Here u^* is the friction velocity equal to 0.0167, κ is the von-Karman constant with value 0.41, and C is a constant equal to 5 corresponding to smooth channel flows (Jimenez, 2004). A mean streamwise turbulence intensity I_0 equal to 12% and integral turbulence length scales of $l_x = 0.56H$, $l_y = 0.33H$, $l_z = 0.25H$ were also measured experimentally.

As inflow condition the velocity profile in Eq. (13) is prescribed and artificial velocity fluctuations are superimposed using the Synthetic Eddy Method adopting the measured anisotropic turbulence characteristics, i.e. intensity and length scales (Jarrin et al., 2009). A convective boundary condition is set at the outlet and the free-surface at the top of the domain is modelled as a shear-free rigid-lid condition. At the bottom and lateral boundary conditions a wall-function is used,

$$\frac{u}{u^*} = \frac{1}{\kappa}\ln\left(Ez^+\right) \tag{14}$$

where u is the velocity at the first grid node off the wall, u^* is the friction velocity, $z^+ = zu^*/\nu$ is the grid resolution in wall units, and E is a constant set to 9 as smooth walls are considered (Launder and Spalding, 1974).

The computational domain keeps an identical cross-section as in the experiments whilst its streamwise length is shortened to 11 m. A two-level local mesh refinement strategy is adopted to have a higher resolution area embedding the turbines, which aids to reduce the computational effort of LES whilst maintaining a high resolution near the turbines. The mesh is uniform in the three spatial directions and two grid resolutions are adopted using local mesh refinement during the validation of the LES-ALM implemented in DOFAS, with values of $\Delta x_i = 0.010$ m and 0.005 m at the finest local resolution region embedding the turbines in the region $-1 < x/D < 15$, $-4 < y/D < 4$, and being these doubled elsewhere. These grid spacings in wall-units considering the experimental friction velocity are $\Delta z^+ \approx 83$ and 42, respectively, which justifies the need for the wall function of Eq. (14). These configurations lead to a total of 19.92 and 53.28 million elements in the coarse and fine meshes, respectively. Considering the turbines have a diameter D equal to 0.27 m, the adopted spatial resolutions equate to 27 and 54 grid divisions along the turbine's diameter, respectively. Such spatial resolution is within the common range of values used in the LES of turbines with ALM (Sørensen et al., 2015) capable of providing a good representation of the dominating large-scale structures in the flow (Yang et al., 2015a). The simulations ran on 51 processors using Supercomputing Wales facilities for 15 days with an equivalent computational load of approx. 18,000 CPUhours.

Constant time step is adopted by attaining a fixed CFL value equal to 0.2 based on the tip speed, i.e. CFL $= \Omega R \Delta t/\Delta x$. Hence, the time steps are $\Delta t \approx 0.0025 D/u_0$ and $0.0017\ D/u_0$ for the coarse and fine meshes respectively, which in turn required about 270 and 420 time steps to compute one turbine revolution. The simulations run for 360 s (900 revolutions considering the front-row turbines) with mean velocities starting to average after the first 40 s of simulation (i.e. 100 turbine revolutions) in order to eliminate initial flow transients. Second-order statistics start to be collected after the simulation of another 100 turbine revolutions, i.e. computed over the final 700 turbine revolutions.

Regarding the geometric characteristics of the devices, turbines are equipped with three blades ($N_b = 3$) whose profile shape are Göttingen 804. As depicted in Fig. 3, the blades are attached to a cylindrical hub of radius equal to 0.01 m and longitudinal length of 0.05 m, which is subsequently connected to a vertical cylinder that joins the rotor with the support structure.

In this work three tidal turbine array configurations are analysed: the first case comprises three turbines aligned in a single row; and the second and third cases comprise two rows of three and four turbines separated $4D$ and $8D$ respectively, which are analysed to quantify the interaction between rows of turbines with varying inter-row spacing. Separation between turbine hubs of those devices in the same row is $D_s = 1.5D$, and devices operated at a constant tip speed ratio of 4.5 at which their performance is maximum, as adopted in the experiments (Stallard et al., 2013; Olczak et al., 2016). Considering every turbine undergoes a different incident velocity, the tip speed ratio of the turbine m, λ_m, is defined as,

$$\lambda_m = \frac{\Omega_m R}{u_{m_0}} \tag{15}$$

where Ω_m is the rotational speed of the m-th turbine, the approach velocity at each of turbine is u_{m_0}, and R is the turbine radius.

Table 1
Turbines rotational speed for the multi-row cases simulated.

Rows separation	Ω_{1r}	Ω_{2r_T}	Ω_{2r_MT}	Ω_{2r_MB}	Ω_{2r_B}
4*D*	15.333	12.724	11.344	11.804	11.651
8*D*	15.333	13.950	12.417	12.417	13.950

From hereinafter, the labelling to the row at which any turbine is "1r" and "2r" referring to the front- or back-row turbines respectively, and the relative position within the row is denoted as "T" top, "B" bottom, "M" middle, "MT" middle-top and "MB" middle-bottom, e.g 2r_MB corresponds to the middle-bottom turbine in the back-row. Table 1 presents the rotational speed of all turbines being that of the front-row turbines uniform, at 15.33 rad/s, and that prescribed to the back-row turbines according to the experiments in Olczak et al. (2016). These are lower than those from the front-row turbines because the back-row devices operate in low-velocity wakes. The time required to perform a full revolution is calculated as $T_i = \Omega_i/2\pi$ and the blade passing frequency, f_0, is equal to $1/(T_i N_b)$.

5. Results and discussion

In this section, the hydrodynamics developed in three different array configurations are firstly discussed to assess on the LES-ALM validation. Further analysis is then performed in the field of time and frequency focusing on the structural loadings experienced by the turbines, e.g. bending moments and forces on the support structure, and fatigue damage equivalent loads.

5.1. Single row of three turbines

Results of the flow past a single row of three turbines with hub-to-hub spacing of 1.5 *D* are presented in Fig. 4 with contours of time-averaged streamwise velocity $\langle u\rangle/u_0$, turbulence intensity u'/u_0, Reynolds shear stress $u'v'/u_0^2$, and ratio of sub-grid scale viscosity over kinematic viscosity ν_{SGS}/ν, which are computed with the fine mesh, i.e. $\Delta x = D/57$. The distribution of streamwise velocity suggests that once the approach flow meets the turbines, it accelerates on the sides of the row and between the turbines as, for this particular case, the close spacing between the turbines favours the local blockage originating a high-velocity bypass flow between them. Fig. 4a depicts the low-momentum wakes behind each device which do not merge into a single wake until 12*D* downstream.

High levels of turbulence intensity are found in the rotor swept area and in the wake extension over which tip vortices travel coherently, as shown in Fig. 4b. In the bypass flow region, levels of u'/u_0 larger than 0.15 are present until 4*D* whilst in the outermost region of the wake, i.e. at $|y/D| \approx 2.25$, turbulence decays below such level at 2*D* as a result of a quicker breakdown of the tip vortices interacting with the ambient flow. Contours of Reynolds shear stress, Fig. 4c, indicate that their maxima are found in the bypass flow regions.

In the LES of wind or tidal turbine farms using the ALM the SGS model plays an important role as the computational meshes are relatively coarse and not all the flow structures are resolved (Martínez-Tossas et al., 2018). Fig. 4d shows that the maximum values of the SGS-to-natural viscosity ratio, ν_{SGS}/ν, are found in the path followed by the tip vortices shed by each turbine reaching values up to approx. 15.

Fig. 5 shows profiles of mean streamwise velocity deficit ($\Delta u = (u_0 - \langle u\rangle)/u_0$) and turbulence intensity predicted by DOFAS with the two meshes and compared with the experimental data of Stallard et al. (2013). At the profile closest to the turbine, the LES-ALM matches the location and value of the lowest velocity deficit regions, i.e. the outer ($|y/D| > 2.25$) and bypass regions, and also achieves a great match of the turbulence intensities. Further downstream, the high-fidelity model also captures the reduction in velocity deficit although at a lower rate than in the experiments as, in profiles at 8*D* or 10*D*, the individual wakes are still discernible from the LESs whilst a single combined wake is developed in the experiments. In terms of turbulence intensity, there is a good agreement found in most of the wake. Despite both meshes providing similar accuracy in predicting the flow dynamics, the fine mesh is adopted in the following analyses as it proved to provide better estimates of the hydrodynamic coefficients (Ouro et al., 2019b).

5.2. Arrays of three and four turbines in two rows

In multi-row arrays, the first row of turbines introduce turbulence into the flow affecting the hydrodynamics of the subsequent rows downstream. Here, a second row of four turbines is placed at two different distances, namely $R_s = 4D$ and 8*D*, behind the front row of three turbines previously analysed. Fig. 6 depicts the arrangement when turbines are separated 4*D* and their labelling.

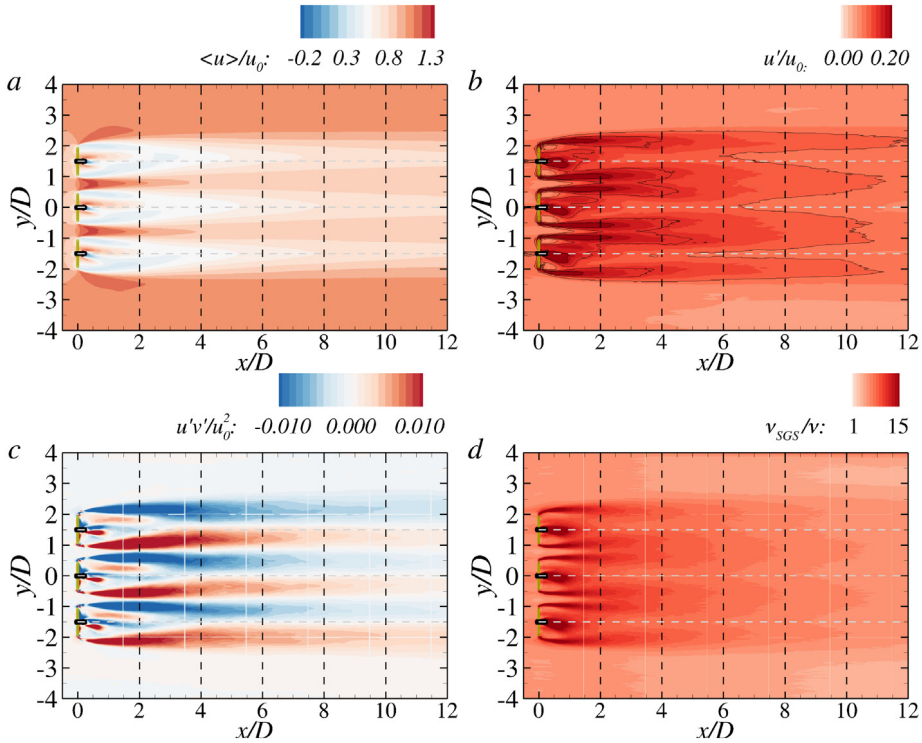

Fig. 4. Results of the three in-line turbines case. Contours of normalised mean (a) streamwise velocities, (b) streamwise turbulence intensity, (c) Reynolds shear stress $u'v'$, and (d) ratio of sub-grid scale (SGS) to kinematic fluid viscosity at hub height.

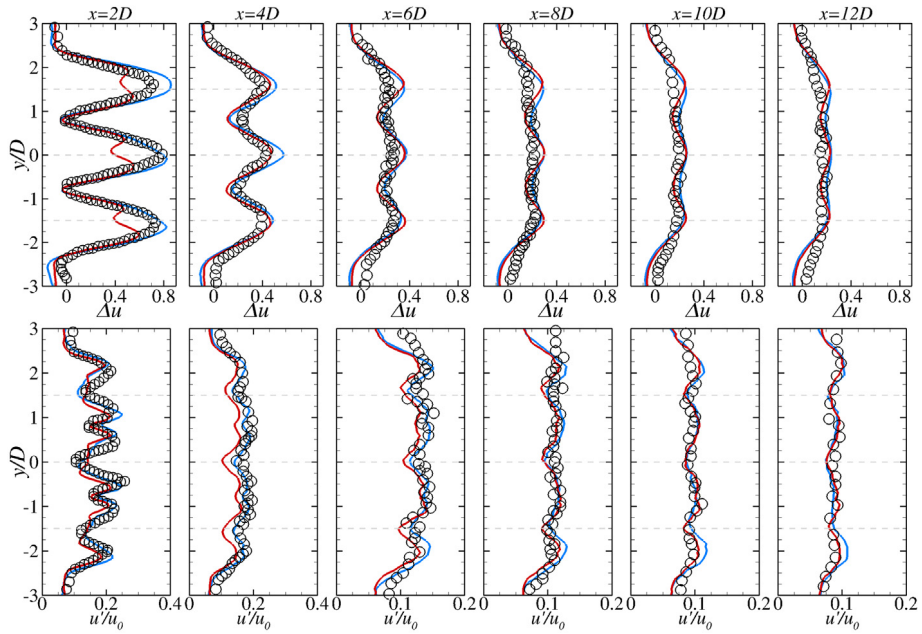

Fig. 5. Profiles of velocity deficit (top) and turbulence intensity (bottom) for the three in-line turbines case. Comparison of experimental data (circles) and LES-ALM results from two mesh resolutions: blue line $\Delta x/D = 27$, red line $\Delta x/D = 54$. (For interpretation of the references to colour in this figure legend, the reader is referred to the web version of this article.)

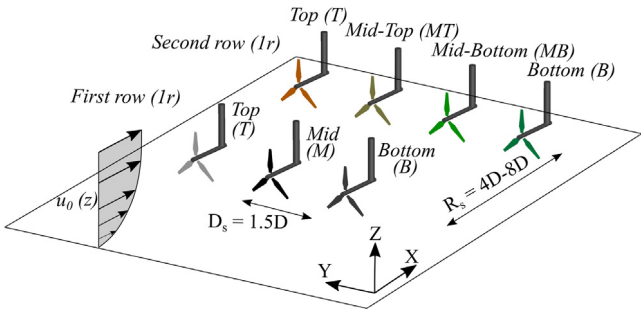

Fig. 6. Array of seven tidal stream turbines placed in two different rows.

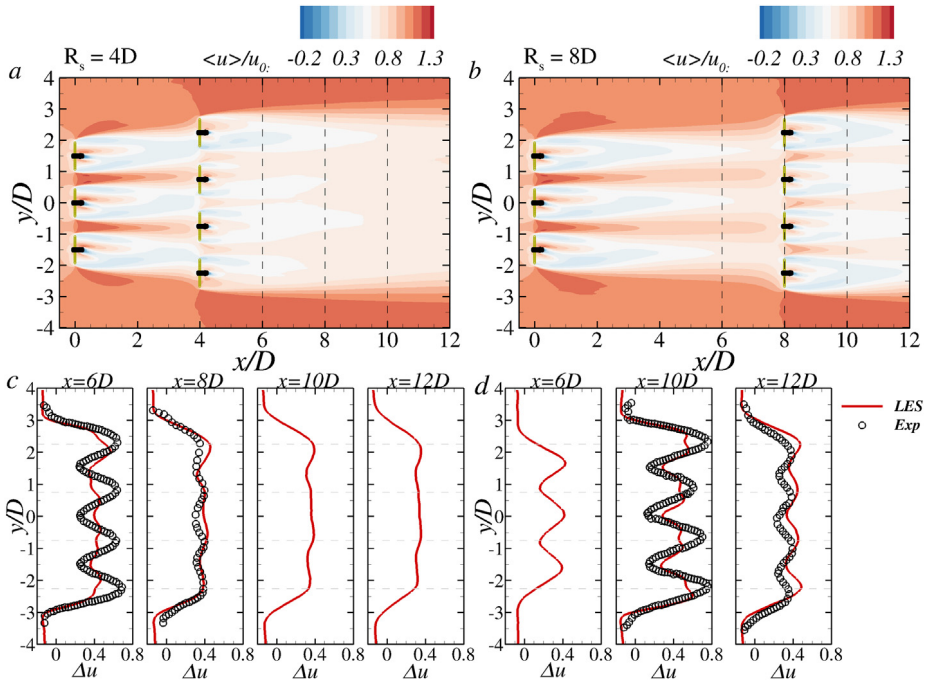

Fig. 7. Results of the two-rows arrays. Contours of mean streamwise velocity for the cases with inter-row separation of (a) 4*D* and (b) 8*D*. Profiles of velocity deficit for the cases with separation of (c) 4*D* and (d) 8*D* comparing LES results and experimental data (Olczak et al., 2016).

Time-averaged hydrodynamics

Results of time-averaged quantities obtained in the simulation of these two-row arrays are presented in Fig. 7 with contours of normalised streamwise velocity and profiles of velocity deficit. For the 4*D* separation case, the turbines in the second-row are greatly influenced by the low-velocity wake generated behind the front turbines. The velocity deficit profiles at distances of $x = 6D$ and 8*D* indicate the LES-ALM captures the lateral extent of the wake whilst the individual wakes at 6*D* are not as well discerned as in the experiments. Shortly further downstream, at $x = 8D$, the computed velocity field is in better agreement with the experiments with a mean wake velocity deficit $\Delta u = 0.4$. These results indicate there is a direct interaction between the rows of turbines and the need for highly accurate eddy-resolving simulations to resolve the near-wake phenomena in the turbines operating in the shadow of another ones. Fig. 7c shows, from the LES-computed velocity profiles at $x = 10D$ and 12*D*, the single merged wake is still visible as full wake recovery is not yet accomplished. In the case with an inter-row spacing of 8*D*, DOFAS achieves a good agreement with experiments for $x = 10D$ and 12*D* in the loci of the maxima and minima of velocity deficit whilst under-predicts their values as the individual wakes from the upstream turbines are not merged into one, as seen in the profile at $x = 6D$.

Fig. 8 shows the contours of streamwise turbulence intensity, turbulent kinetic energy and Reynolds shear stress in a plane at hub height for the two multi-row analysed cases, which allows to compare the array hydrodynamics when different row spacings are adopted. For the 4*D* separation case, the back-row turbines operate in a highly turbulent wake with an average value of $u' = 0.2u_0$ (see Fig. 5b) whereas with a spacing of 8*D* turbulence intensity reduce to

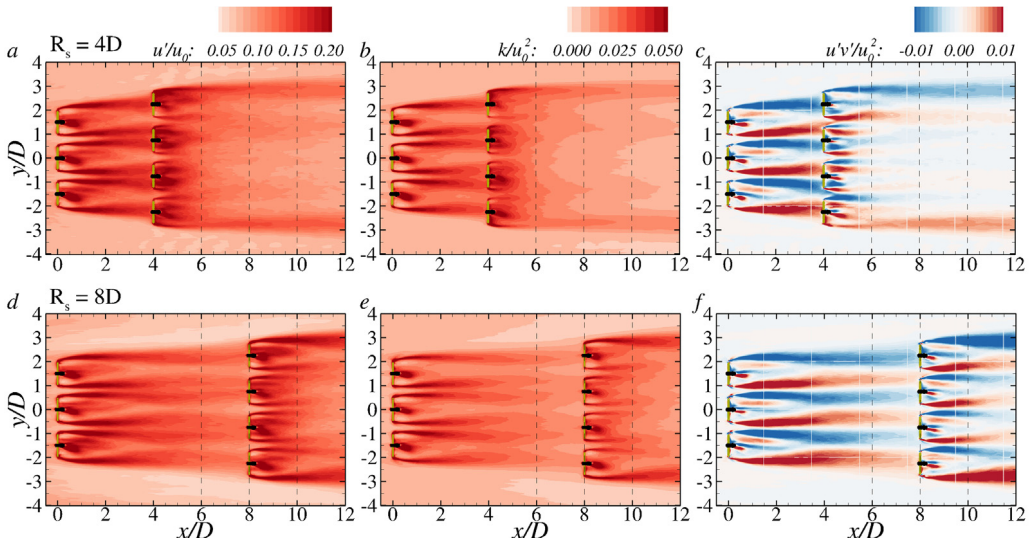

Fig. 8. Contours of normalised (a and d) streamwise turbulence intensity, (b and e) turbulence kinetic energy and (c and f) Reynolds shear stress for the two arrays of turbines with an inter-row separation of 4*D* (top) and 8*D* (bottom) at hub height.

similar values to those found in the inflow condition, i.e. $u' = 0.1u_0$. Fig. 8a show the turbines 2r-T and 2r-B partially operate in the highly turbulent wake of the upstream turbines and are also influenced by free-stream flow. Hence, the outermost turbines in the back-row operate in the highly-turbulent low-momentum wake and high-momentum ambient flow featuring moderate turbulent intensities. The middle turbines in the second row, i.e. 2r-MB and 2r-MT, develop wakes with high levels of turbulence close to the turbine but these rapidly decay after 2D downstream, i.e. at $x = 10D$. Contours of turbulent kinetic energy (k), Fig. 8b, further supports the observation that turbulence rapidly decays after a distance of 2*D* in the wake behind the second-row inner turbines, which is laterally bounded by the shear-layers originated by the outermost turbines exhibiting high levels of turbulence.

Reynolds shear stress distribution significantly change for the different arrays analysed, as shown in Fig. 8c and e. The values of $u'v'$ behind the front-row turbines are the largest as a result of the momentum exchange between tip vortices and high-momentum bypass flow and the loss of coherence of the latter. For a short row separation of 4*D*, the wake downstream of the back-row turbines develop relatively small Reynolds shear stresses as they face a less energetic flow than the front-row turbines, reducing momentum exchange. Nonetheless, the outermost turbines partly operate under free-stream flow with which their tip vortices interact and trigger $u'v'$ values for a distance larger than 8*D* downstream, as seen in Fig. 8c. The flow hydrodynamics presented in Fig. 8 evidence the large interaction between the different rows in the case with a narrow spacing of 4*D* which reduce when increasing to 8*D* the inter-row distance.

Instantaneous flow field

Fig. 9 shows iso-surfaces of vorticity magnitude and contours of instantaneous streamwise velocities at a horizontal plane at hub height for the two different multi-row configurations. One of the main consequences of adopting relatively narrow inter-row separation is that the energetic flow structures generated by front-row turbines impinge back-row turbines. In both configurations, the tip vortices generated at the blades' tip are well-captured by the LES-ALM transitioning to their breakdown into small-scale structures after $1-2D$ behind the turbines. For the narrowest separation case, i.e. 4*D*, Fig. 9 presents how the energetic turbulent structures impact the second-row turbines whilst in the 8*D* separation case these decayed to small-scale turbulence. It is worth noting that in Fig. 9, an equal spacing between the tip vortices is observed for the front-row turbines (Ouro et al., 2017) whilst those from turbines in the second-row are slightly distorted as a result of the disturbed approach flow conditions.

Further insight into the instantaneous flow behaviour in the tidal farm with a row spacing (R_s) of 4*D* is given in Fig. 10 with contours of streamwise velocities at six time-frames spaced 3.9 s apart each other, which is equivalent to 1.6 times a full revolution of a front-row turbine ($T_{1r} \approx 2.44$ s). The wake behind the turbines is characterised by the presence of tip vortices, support structure wake and low-velocity near-wake. Comparing the different snapshots, LES captures the low-frequency oscillation of the bypass flow region generated from the high local blockage of the narrow-spaced first-row turbines. This high-velocity region behaves like a jet and, once the tip vortices from the first turbines lose coherence, it develops a transversal oscillation impinging the back-row turbines, as seen comparing the instantaneous flow amongst the multiple time-frames shown in Fig. 10. This phenomenon is reduced in the subsequent row of turbines as the flow velocity at their location is considerably lower than the bulk velocity and then devices do not generate as much blockage

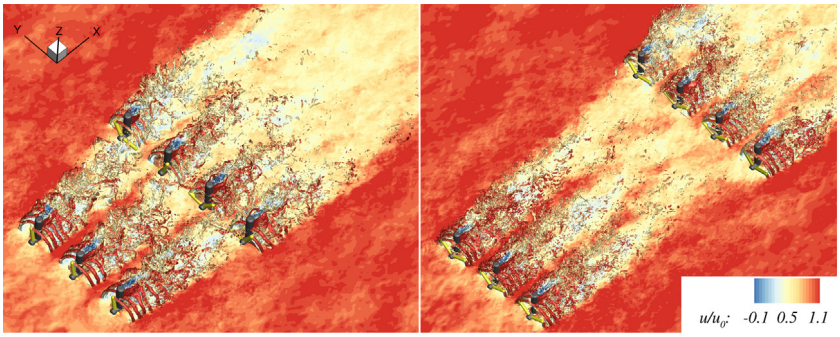

Fig. 9. Instantaneous flow generated in the two-row arrays *i*th separation of 4*D* (left) and 8*D* (right) between rows using iso-surfaces of vorticity $|\omega|D/u_0 = 12.5$ and contours of instantaneous streamwise velocity at hub height.

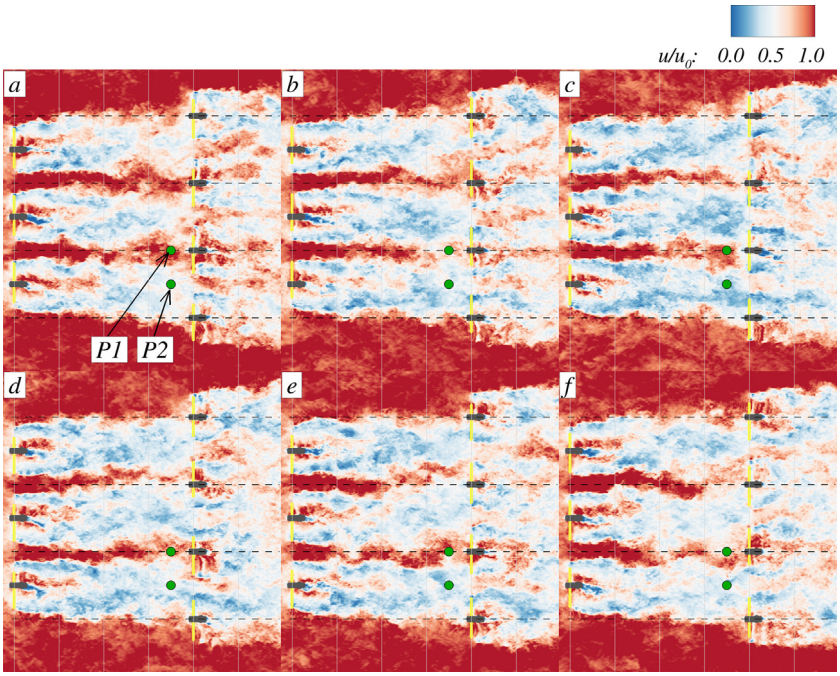

Fig. 10. Snapshots of contours of instantaneous streamwise velocity at 6 different time instants each 3.9s or 1.6 full revolutions apart. P1 and P2 are location from which velocity samples are collected.

as those in the first row. Due to the narrow separation of 4*D* between the two rows of turbines, the flow approaching the back row is remarkably unsteady with large velocity deficit causing their wakes lack of coherent tip vortices signature (see Fig. 9) or bypass flow. The outermost turbines (2r-T, 2r-B) partially face the high-momentum ambient flow and low-velocity wake which causes an uneven load distribution in the support structure.

Spectral analysis of time series of streamwise velocity fluctuation (u') are computed from the samples obtained at locations depicted in Fig. 10, namely P1 which is just upstream of the turbine 2r-MB aligned with its hub and P2 which is aligned with the hub from the turbine 1r-B. These locations are selected as P1 allows to characterise the bypass flow oscillation frequency and P2 lies in the wake meandering from the upstream turbines. The analysis is done for 4*D* and 8*D* separation cases, i.e. P1 and P2 are at $x = 3.8D$ and $7.8D$, respectively. Fig. 11 presents the pre-multiplied spectra with frequencies normalised by the blade passing frequency (f_0) obtained at both locations in the two arrays. At P1 with row separation of 4*D*, the highest spectral energy is found for frequencies in the order of $f \approx 0.1 - 0.3f_0$ corresponding to the low-frequency oscillation of the jet-like bypass flow whereas, at P2, energy peaks are not observed at that frequency range. At the former point, however, a peak is discerned at $f \approx 0.7f_0$ linked to wake effects from the upstream turbine such as hub vortex or wake meandering. The spectra at the two selected locations in the 8*D* separation case feature a peak associated to the wake meandering at $f \approx 0.7f_0$ with a larger spectral energy than that observed for the 4*D* inter-row separation case at P2. This indicates low-frequency effects are enhanced with increasing distance between rows. No peaks

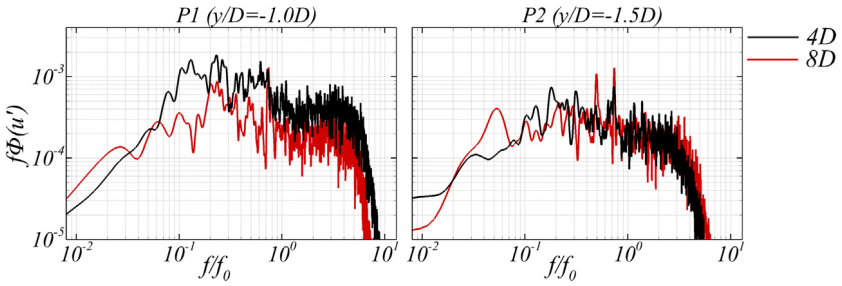

Fig. 11. Pre-multiplied power spectral density of streamwise velocity fluctuations $\Phi(u')$ obtained at two locations for the cases with separation between rows of 4*D* and 8*D*.

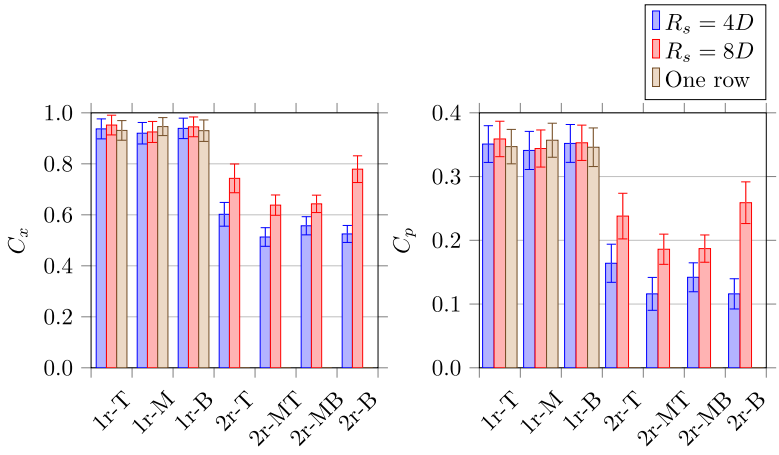

Fig. 12. Mean values and root-mean-square of (a) thrust and (b) power coefficients for the different turbines from the configurations analysed: one row and two rows separated 4*D* and 8*D*.

at the blade passing frequency are found in any of the spectra as can be expected at such distances downstream of the first turbines (Ouro and Stoesser, 2019). The Strouhal number associated to the wake meandering, $St = fD/u_0$, is equal to 0.17 similarly to the value of 0.15 obtained by Foti et al. (2018) at a distance of $x = 5D$ in the geometry-resolved large-eddy simulation of a wind turbine.

5.3. Rotor loadings

One relevant aspect in the design of tidal stream turbine arrays is the maximisation of the entire farm power generation. The performance of the turbines is presented in Fig. 12 with values of thrust and power coefficients. For a single row of turbines, the operating devices attain a similar value of $C_x \approx 0.93$ and $C_p \approx 0.35$, which are slightly overestimated compared to the experimental value $C_x^{exp} \approx 0.86$ (Olczak et al., 2016). The second-row of turbines undergo lower hydrodynamic coefficients values which can be expected as they operate in a region with notably higher velocity deficit, Fig. 8. For the 4*D* separation case, their C_x value drop to a mean of 0.55 and, more importantly, their power coefficient reduces to an average of 0.135, which means that these devices are 50% less efficient than the front-row turbines considering free-stream flow velocity. Increasing the row separation to 8*D*, C_x of back-row turbines attain values 0.64 and 0.75 for the inner and outermost turbines respectively, with power coefficients of 0.19 and 0.25. The hydrodynamic coefficients also reflect that back-row outermost turbines, i.e. 2r-T and 2r-B, are partly exposed to the fast-flowing ambient flow exhibiting larger coefficient values, whilst the back-row inner turbines undergo lower forces as they are embedded into the low-momentum wake from the front-row turbines (Ouro et al., 2019b). Note that the current turbulence intensity level of 12% at the inlet is representative of that at tidal sites, e.g. Harrold and Ouro (2019) and Milne et al. (2016), so the current negative interaction between turbines in secondary rows could be enhanced under lower levels of turbulence intensities due to a slower wake recovery (Mycek et al., 2014b).

To ensure of resilience tidal turbines there is a need for determining the extreme loadings they are likely to be subjected to avoiding sudden failure or unscheduled maintenance. In Fig. 13 the probability of exceedance of thrust, flapwise and edgewise bending moments is presented for the seven turbines from multi-row cases. The front turbines experience the largest values of thrust as they face the unperturbed energetic free-stream flow. Thrust loads in the back-row turbines

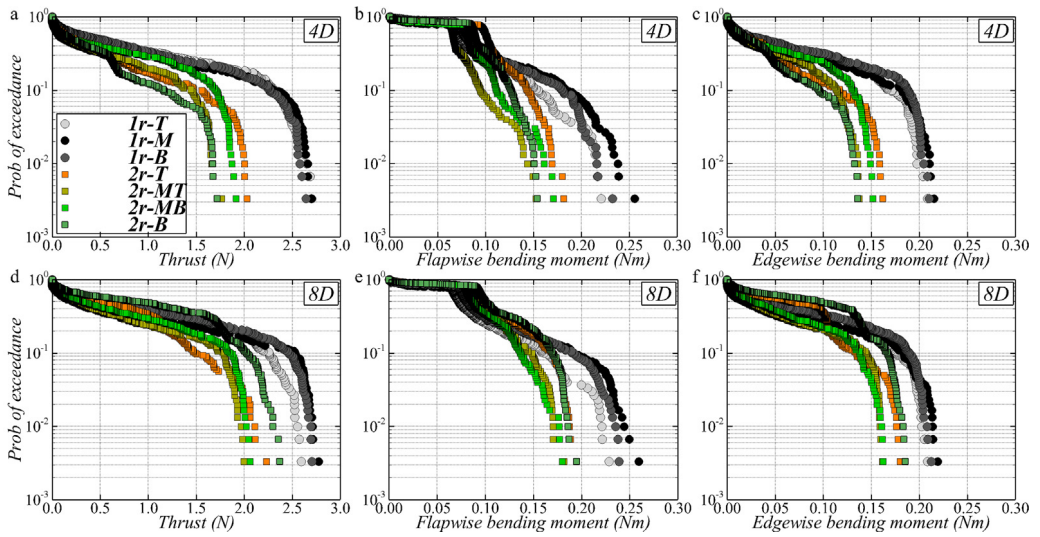

Fig. 13. Probability of exceedance of thrust, flapwise and edgewise bending moments for the cases with inter-row separation of (a–c) 4*D* and (d–f) 8*D*.

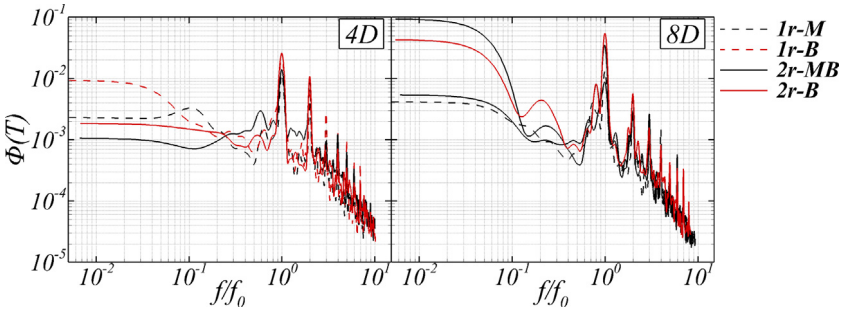

Fig. 14. Power spectral density of thrust and flapwise bending moment for the two cases with multiple rows.

notably increase with inter-row spacing which results from larger momentum recovery. Analogously, the largest bending moment values are found in those turbines at the front and there is a small variation for the back-row turbines when increasing row spacing.

Fig. 14 analyses in the domain of frequency the periodicity of the phenomena contributing to the temporal changes in thrust (T) and flapwise bending moment (M_f) for the two-rows cases, with the frequencies normalised by the blade passing frequency. For both arrays, energy peaks in spectral density are observed at $f/f_0 = 1$ and harmonics of it, which indicates that the variation of these loads depends on the turbine's rotational dynamics and less on the oncoming turbulence. These peaks are more pronounced for the outermost turbines in both front and rear rows, i.e. 1r-B and 2r-B, although this is more remarkable for the former turbine suggesting the variation of thrust and bending moments are larger on back-row turbines.

5.4. Support structure loadings

The probability of exceedance of yaw, *x*- and *y*-moments on the support structure of each turbine are presented in Fig. 15. The outermost turbines in the back row experience the largest yaw moments as a result of the imbalance caused by their exposure to both high-velocity free-stream flow and low-velocity upstream-turbine wakes, attaining maximum values up to twice larger than any other turbine. These results suggest that, despite increasing the inter-row spacing from 4*D* to 8*D*, yaw-moment load-imbalance due to turbine-wake interaction effects persist on 2r-T and 2r-B turbines. Considering tower moments, front-row turbines seem to suffer the largest values as they face the high momentum of the free-stream flow. Interestingly, values of M_{twr_X} and M_{twr_Y} on the back-row turbines increase with larger spacing as a consequence of more momentum being recovered before the flow impinges these devices.

The power spectral energy of M_{yaw} for four different turbines from both multi-row arrays is plotted in Fig. 16, showing that the frequency associated with the largest energy peak is at $3f_0$, which indicates the oscillation of yaw moment relates

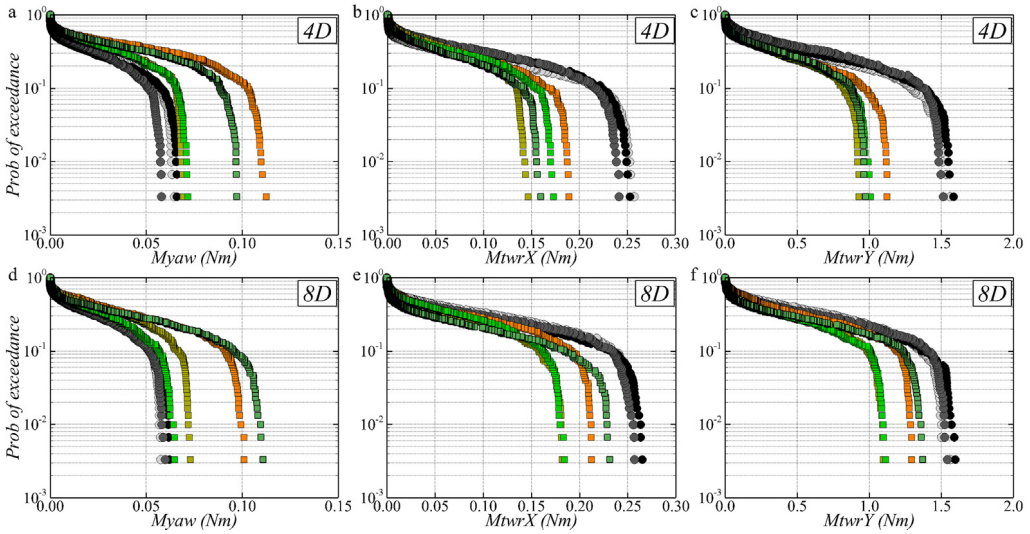

Fig. 15. Probability of exceedance of yaw moment, and x- and y-tower moments on the supporting structure for the cases with inter-row separation of (a–c) 4D and (d–f) 8D. See legend of Fig. 13.

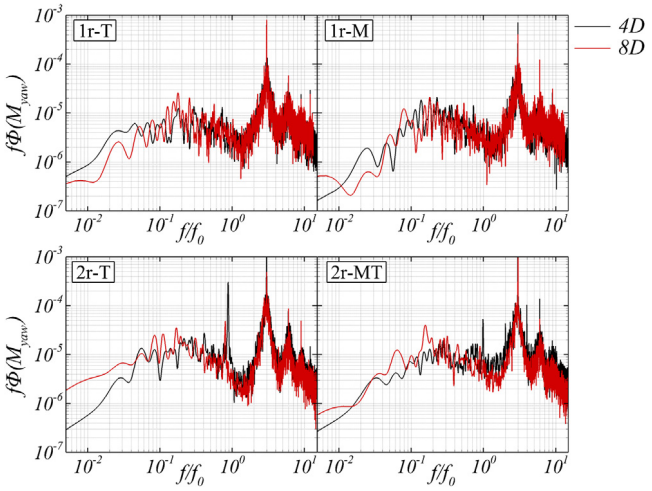

Fig. 16. Pwelch of the yaw moment from four different turbines considering the two multiple-rows arrays simulated.

to the rotation of the three blades. Noteworthy is a secondary energy peak observed at a frequency of approx. $0.85f_0$ for the rear turbines which is attributed to the low-frequency motion of the front-turbines' wakes and bypass flow impinging the back-row turbines. Such effect is most noticeable for the outermost turbines, e.g. 2r-T, although such wake-turbine interaction phenomenon decreases when placing the second row of turbines at 8D as the energy associated to the peak at $f = 0.85p$ diminishes for the 2r-T turbine and even vanishes for the 2r-MT device.

5.5. Fatigue damage analysis

Quantification of the fatigue loads is needed to ensure the integrity of the turbines in the long-term. Here, the fatigue damage is analysed from time-series of the forces computed with the ALM with the aim of determining the Damage Equivalent Load (DEL) (McCann, 2007). Firstly, the instantaneous loads are binned using a rainflow counting method and stress range histograms are obtained indicating the number of times a given load occurs. Then, the Palmgren–Miner rule is applied with a Goodman correction that defines a relationship between mean load (or stress) and alternating load (or stresses) values, and which is required for non-zero mean loadings. The calculated DEL determines the representative load that causes a fatigue damage over the simulated turbine revolutions equivalent to that from the load spectrum with different values each acting a finite number of cycles (Barradas-Berglind and Wisniewski, 2016). The single damage

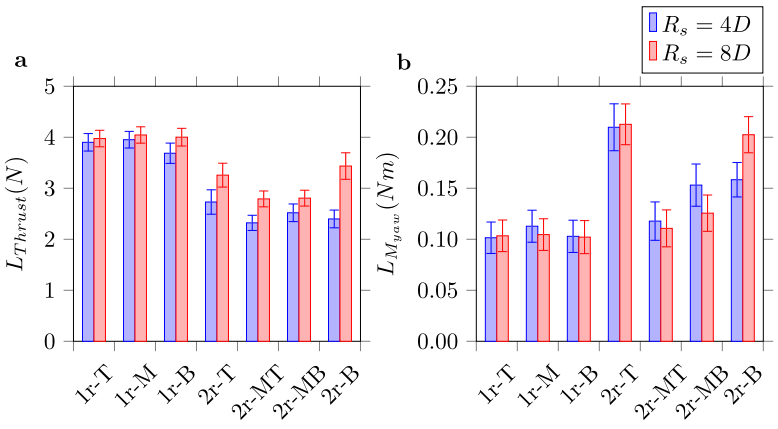

Fig. 17. Damage Equivalent Loads of thrust and tower yaw moment for the seven turbines in the multiple row configurations analysed. Error bars indicate root-mean-square values.

equivalent load, L_N, can be written as,

$$L_N = \sqrt[m]{\frac{\sum_{i=1}^{bins} n_i \cdot F_i^m}{N}} \tag{16}$$

where i refers to the bin number, n_i and F_i are the number of cycles and mean load value of the ith-bin, m is the slope of the S–N curve (Wöhler exponent), and N is the simulated number of cycles calculated as the total simulation time over the period of a single turbine revolution. When loadings on the blades are considered m is equal to 10 corresponding to a composite material, whereas for tower-loadings m is 4 corresponding to steel (Mullings and Stallard, 2018). The number of bins is equal to 60.

Results of the thrust DEL on a single blade computed for every turbine are presented in Fig. 17. Front-row turbines undergo larger thrust fatigue loads than those in the rear row as the former face higher flow speeds whilst the latter operate in regions of lower but more turbulent flow velocities, increasing the fluctuation frequency of thrust but with reduced load values. Additionally, the back-row turbines rotate a lower amount of revolutions also contributing to lower thrust DEL (Lee et al., 2013). The increase in R_s from $4D$ to $8D$ results in larger thrust DELs on the back-row turbines as they operate in a higher momentum flow with increasing spacing. M_{yaw} DEL presented in Fig. 17 shows back-row turbines achieve the largest values due to the faced flow asymmetry. This is more noticeable for the outermost turbines 2r-T and 2r-B experiencing nearly double $L_{M_{yaw}}$ value than first-row turbines, as a result of being partially affected by wake-shadowing effects and undisturbed ambient flow. Furthermore, fluctuation of $L_{M_{yaw}}$ values in second-row turbines increase approximately 10% when $R_s = 4D$ than when $8D$ is adopted. Hence, turbines experience different long-term M_{yaw} fatigue loads depending on the layout configuration.

Fig. 18 presents the distribution of fatigue loads for torque, flapwise bending moment and x- and y-tower moments. The distribution of the damage equivalent loads among the different turbines for these quantities is similar to those seen for the thrust in Fig. 17a, which indicate these DELs for the outermost back-row turbines are less influenced by their partial exposure to the low-velocity wakes and high-speed ambient flow.

6. Conclusions

The design of resilient arrays of tidal stream turbines requires to understand and quantify the complex interaction between turbines, their wakes and the ambient turbulent flow. This paper identifies the main hydrodynamics developed in seven-turbine arrays investigating the effect of inter-row spacing, adopting the large-eddy simulation approach coupled with an actuator line model which allowed the quantification of the loadings on the devices. The proposed Digital OFfshore FArm Simulator (DOFAS) was validated with experimental data for the three configurations analysed and showed a good agreement in both first and second order flow statistics.

Analysis of the mean wake recovery with three in-line turbines showed that the merging between individual wakes into a single combined structure was observed to take place at about 10 to 12 diameters downstream, when turbulence introduced by the turbines decayed to similar values to the free-stream conditions. This far-field effect was observed in the simulation of the seven-turbine arrays, with spacing of 4 and 8 diameters (D) between rows, as wake shadowing effects caused detrimental performance in the back-row turbines. Increasing the separation from 4D to 8D allowed the rear turbines to be more efficient but these are yet about 30% less efficient that those in the front-row, which suggests that larger row spacings may be required. An immediate effect of a narrow separation between rows is that tip vortices

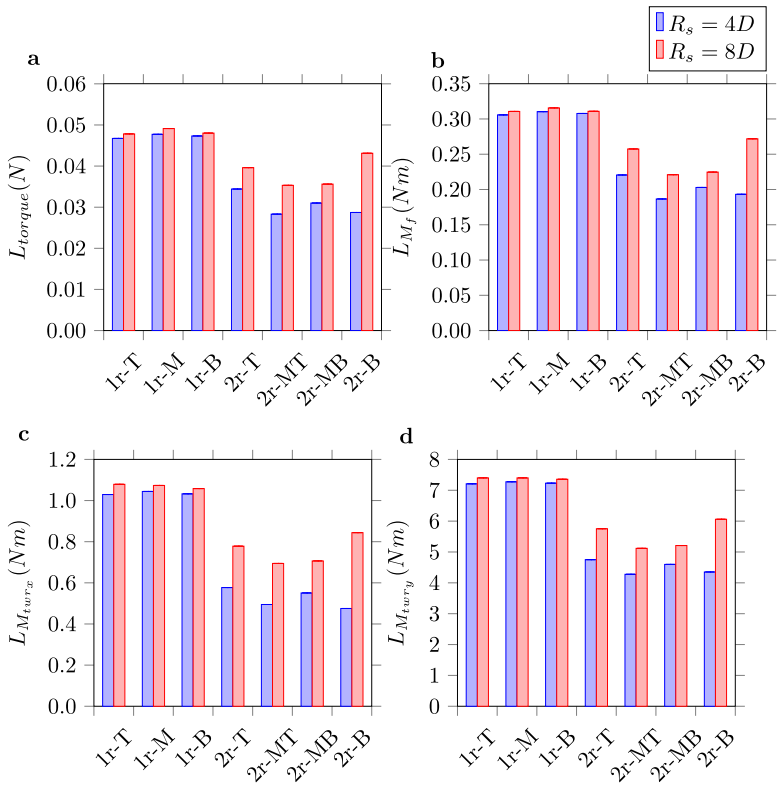

Fig. 18. Damage Equivalent Loads of (a) torque, (b) flapise bending moment, (c) *x*- and (d) *y*-tower moments for the seven turbines in the multiple row configurations analysed.

shed from front-row turbines can impinge the back row devices triggering unsteadiness, however this diminished when adopting a spacing of 8D.

The maximum loadings experienced by the turbines were calculated based on their probability of being exceeded. Rotor loadings, e.g. thrust, flapwise and edgewise bending moments, are larger in the front row turbines as a result of them facing a higher momentum flow. The former loadings on the back-rows increased when a larger spacing was adopted. Interestingly, tower yaw moments were largest on the back-row outermost turbines as these partially faced low-momentum wakes and high-momentum ambient flow, with the former effect identified from a peak at a frequency lower than the turbine rotational frequency in the load spectra, which only appeared on those turbines. Probability of exceedance of tower moments in streamwise and cross-flow directions showed analogous distribution to that of rotor loadings, i.e. being largest on the front-row turbines.

Fatigue loads on the turbines were determined in terms of damage equivalent load. The front-row turbines experience the largest fatigue from thrust, bending moments and *x*- and *y*-tower moments. Increasing the row spacing from 4*D* to 8*D* caused the back-row turbines to operate in a region of higher momentum, thus fatigue loads increased. However, the results for the yaw moment indicate back-row turbines suffered the largest fatigue loads being this more noticeable on the outermost turbines.

Overall, the LES-ALM results evidenced that an inter-row spacing of 4*D* is deemed too short as the wake deficit is still large and back-row turbines have very low efficiency. A spacing of 8*D* appeared not enough either as the back-row turbines still had a low efficiency and were subject to increased fatigue loadings. The presented Digital OFfshore FArm Simulator has demonstrated to be a suitable and computationally efficient tool to design and study tidal turbine arrays. Future research will expand to larger number of turbines and rows operating in different flow conditions, such as incident angle or water depths.

Acknowledgements

The authors would like to acknowledge the support of the Supercomputing Wales project, which is part-funded by the European Regional Development Fund (ERDF) via the Welsh Government. This research was partially supported by the UK Engineering and Physical Sciences Research Council (EPSRC) under the grant number EP/R51150X/1, and the Ministerio de Ciencia, Innovación y Universidades of the Spanish Government (grant #RTI2018-093366-B-I00). Information on the

data underpinning the results presented here, including how to access them, can be found in the Cardiff University data catalogue at 10.17035/d.2019.0083917166.

References

Abolghasemi, M.A., Piggott, M.D., Spinneken, J., Vire, A., Cotter, C.J., Crammond, S., 2016. Simulating tidal turbines with multi-scale mesh optimisation techniques. J. Fluids Struct. 66, 69–90. http://dx.doi.org/10.1016/j.jfluidstructs.2016.07.007.

Afgan, I., McNaughton, J., Rolfo, S., Apsley, D.D., Stallard, T., Stansby, P., 2013. Turbulent flow and loading on a tidal stream turbine by LES and RANS. Int. J. Heat Fluid Flow 43, 96–108. http://dx.doi.org/10.1016/j.ijheatfluidflow.2013.03.010.

Ahmadian, R., Falconer, R., 2012. Assessment of array shape of tidal stream turbines on hydro-environmental impacts and power output. Renew. Energy 44, 318–327. http://dx.doi.org/10.1016/j.renene.2012.01.106.

Apsley, D.D., Stallard, T., Stansby, P.K., 2018. Actuator-line CFD modelling of tidal-stream turbines in arrays. J. Ocean Eng. Mar. Energy 4 (4), 259–271. http://dx.doi.org/10.1007/s40722-018-0120-3.

Baba-Ahmadi, M.H., Dong, P., 2017. Validation of the actuator line method for simulating flow through a horizontal axis tidal stream turbine by comparison with measurements. Renew. Energy 113, 420–427. http://dx.doi.org/10.1016/j.renene.2017.05.060.

Barradas-Berglind, J.J., Wisniewski, R., 2016. Representation of fatigue for wind turbine control. Wind Energy 19 (12), 2189–2203. http://dx.doi.org/10.1002/we.1975, arXiv:arXiv:1006.4405v1.

Bomminayuni, S., Stoesser, T., 2011. Turbulence statistics in an open-channel flow over a rough bed. J. Hydraul. Eng. 137 (11), 1347–1358. http://dx.doi.org/10.1061/(ASCE)HY.1943-7900.0000454.

Cal, R.B., Lebrón, J., Castillo, L., Kang, H.S., Meneveau, C., 2010. Experimental study of the horizontally averaged flow structure in a model wind-turbine array boundary layer. J. Renew. Sustain. Energy 2 (1), 013106. http://dx.doi.org/10.1063/1.3289735.

Cevheri, M., McSherry, R., Stoesser, T., 2016. A local mesh refinement approach for large-eddy simulations of turbulent flows. Internat. J. Numer. Methods Fluids 82, 261–285. http://dx.doi.org/10.1002/fld.421.

Chawdhary, S., Hill, C., Yang, X., Guala, M., Corren, D., Colby, J., Sotiropoulos, F., 2017. Wake characteristics of a TriFrame of axial-flow hydrokinetic turbines. Renew. Energy 109, 332–345. http://dx.doi.org/10.1016/j.renene.2017.03.029.

Chorin, A.J., 1968. Numerical solution of the Navier-Stokes equations. Math. Comp. 22 (104), 745–762. http://dx.doi.org/10.1090/S0025-5718-1968-0242392-2.

Churchfield, M.J., Lee, S., Michalakes, J., Moriarty, P.J., 2012. A numerical study of the effects of atmospheric and wake turbulence on wind turbine dynamics. J. Turbul. 13, 1–32. http://dx.doi.org/10.1080/14685248.2012.668191.

Churchfield, M.J., Li, Y., Moriarty, P.J., 2013. A large-eddy simulation study of wake propagation and power production in an array of tidal-current turbines.. Philos. Trans. A. Math. Phys. Eng. Sci. 371 (1985), 20120421. http://dx.doi.org/10.1098/rsta.2012.0421.

Draper, S., Nishino, T., 2014. Centred and staggered arrangements of tidal turbines. J. Fluid Mech. 739, 72–93. http://dx.doi.org/10.1017/jfm.2013.593.

Foti, D., Yang, X., Guala, M., Sotiropoulos, F., 2016. Wake meandering statistics of a model wind turbine: Insights gained by large eddy simulations. Phys. Rev. Fluids 1 (4), 044407. http://dx.doi.org/10.1103/PhysRevFluids.1.044407.

Foti, D., Yang, X., Sotiropoulos, F., 2018. Similarity of wake meandering for different wind turbine designs for different scales. J. Fluid Mech. 842, 5–25. http://dx.doi.org/10.1017/jfm.2018.9.

Funke, S.W., Kramer, S.C., Piggott, M.D., 2015. Design optimisation and resource assessment for tidal-stream renewable energy farms using a new continuous turbine approach. Renew. Energy 99, 1046–1061. http://dx.doi.org/10.1016/j.renene.2016.07.039, arXiv:1507.05795.

Garrett, C., Cummins, P., 2007. The efficiency of a turbine in a tidal channel. J. Fluid Mech. 588 (2007), 243–251. http://dx.doi.org/10.1017/S0022112007007781.

Harrold, M., Ouro, P., 2019. Rotor loading characteristics of a full-scale tidal turbine. Energies 6, 1035. http://dx.doi.org/10.3390/en12061035.

Jarrin, N., Prosser, R., Uribe, J.-C., Benhamadouche, S., Laurence, D., 2009. Reconstruction of turbulent fluctuations for hybrid RANS/LES simulations using a Synthetic-Eddy Method. Int. J. Heat Fluid Flow 30 (3), 435–442. http://dx.doi.org/10.1016/j.ijheatfluidflow.2009.02.016.

Jimenez, J., 2004. Turbulent flows over rough walls. Annu. Rev. Fluid Mech. 36 (1), 173–196. http://dx.doi.org/10.1146/annurev.fluid.36.050802.122103.

Kang, S., Borazjani, I., Colby, J.A., Sotiropoulos, F., 2012. Numerical simulation of 3D flow past a real-life marine hydrokinetic turbine. Adv. Water Resour. 39, 33–43. http://dx.doi.org/10.1016/j.advwatres.2011.12.012.

Kang, S., Yang, X., Sotiropoulos, F., 2014. On the onset of wake meandering for an axial flow turbine in a turbulent open channel flow. J. Fluid Mech. 744, 376–403. http://dx.doi.org/10.1017/jfm.2014.82.

Kara, S., Kara, M.C., Stoesser, T., Sturm, T.W., 2015. Free-surface versus rigid-lid LES computations for bridge-abutment flow. J. Hydraul. Eng. 141 (9), 04015019. http://dx.doi.org/10.1061/(ASCE)HY.1943-7900.0001028.

Launder, B., Spalding, D., 1974. The numerical computation of turbulent flows. Comput. Methods Appl. Mech. Engrg. 3, 269–289. http://dx.doi.org/10.1016/0045-7825(74)90029-2.

Lee, S., Churchfield, M.J., Moriarty, P.J., Jonkman, J., Michalakes, J., 2013. A numerical study of atmospheric and wake turbulence impacts on wind turbine fatigue loadings. J. Sol. Energy Eng. 135 (3), 031001. http://dx.doi.org/10.1115/1.4023319.

Magagna, D., Uihlein, A., 2015. Ocean energy development in Europe: Current status and future perspectives. Int. J. Mar. Energy 11, 84–104. http://dx.doi.org/10.1016/j.ijome.2015.05.001.

Martínez-Tossas, L.A., Churchfield, M.J., Yilmaz, A.E., Sarlak, H., Johnson, P.L., Sørensen, J.N., Meyers, J., Meneveau, C., 2018. Comparison of four large-eddy simulation research codes and effects of model coefficient and inflow turbulence in actuator-line-based wind turbine modeling. J. Renew. Sustain. Energy 10 (3), http://dx.doi.org/10.1063/1.5004710.

Masters, I., Williams, A., Croft, T.N., Togneri, M., Edmunds, M., Zangiabadi, E., Fairley, I., Karunarathna, H., 2015. A comparison of numerical modelling techniques for tidal stream turbine analysis. Energies 8 (8), 7833–7853. http://dx.doi.org/10.3390/en8087833.

McCann, G., 2007. Tidal current turbine fatigue loading sensitivity to waves and turbulence – a parametric study. In: Proc. 7th Eur. Wave Tidal Energy. Porto, Portugal.

McSherry, R., Chua, K., Stoesser, T., Mulahasan, S., 2018. Free surface flow over square bars at intermediate relative submergence. J. Hydraul. Res. 56 (6), 825–843. http://dx.doi.org/10.1080/00221686.2017.1413601.

Mehta, D., van Zuijlen, A.H., Koren, B., Holierhoek, J.G., Bijl, H., 2014. Large Eddy Simulation of wind farm aerodynamics: A review. J. Wind Eng. Ind. Aerodyn. 133, 1–17. http://dx.doi.org/10.1016/j.jweia.2014.07.002.

Milne, I.A., Day, A.H., Sharma, R.N., Flay, R.G.J., 2016. The characterisation of the hydrodynamic loads on tidal turbines due to turbulence. Renew. Sustain. Energy Rev. 56, 851–864. http://dx.doi.org/10.1016/j.rser.2015.11.095.

Mullings, H., Stallard, T., 2018. Unsteady loading in a tidal array due to simulated turbulent onset flow. In: 3rd Int. Conf. Renew. Energies Offshore. Lisbon, Portugal.

Musa, M., Hill, C., Sotiropoulos, F., Guala, M., 2018. Performance and resilience of hydrokinetic turbine arrays under large migrating fluvial bedforms. Nat. Energy 3, 839–846. http://dx.doi.org/10.1038/s41560-018-0218-9.

Mycek, P., Gaurier, B., Germain, G., Pinon, G., Rivoalen, E., 2014a. Experimental study of the turbulence intensity effects on marine current turbines behaviour. Part I: One single turbine. Renew. Energy 66, 729–746. http://dx.doi.org/10.1016/j.renene.2013.12.036.

Mycek, P., Gaurier, B., Germain, G., Pinon, G., Rivoalen, E., 2014b. Experimental study of the turbulence intensity effects on marine current turbines behaviour. Part II: Two interacting turbines. Renew. Energy 68, 876–892. http://dx.doi.org/10.1016/j.renene.2013.12.048.

Myers, L.E., Bahaj, A.S., 2012. An experimental investigation simulating flow effects in first generation marine current energy converter arrays. Renew. Energy 37 (1), 28–36. http://dx.doi.org/10.1016/j.renene.2011.03.043.

Nash, S., Phoenix, A., 2017. A review of the current understanding of the hydro-environmental impacts of energy removal by tidal turbines. Renew. Sustain. Energy Rev. 80, 648–662. http://dx.doi.org/10.1016/j.rser.2017.05.289.

Nicoud, F., Ducros, F., 1999. Subgrid-scale stress modelling based on the square of the velocity gradient tensor. Flow, Turbul. Combust. 62 (3), 183–200. http://dx.doi.org/10.1023/A:1009995426001.

Olczak, A., Stallard, T., Feng, T., Stansby, P.K., 2016. Comparison of a RANS blade element model for tidal turbine arrays with laboratory scale measurements of wake velocity and rotor thrust. J. Fluids Struct. 64, 87–106. http://dx.doi.org/10.1016/j.jfluidstructs.2016.04.001.

Ouro, P., Fraga, B., Lopez-Novoa, U., Stoesser, T., 2019a. Scalability of an Eulerian-Lagrangian large-eddy simulation solver with hybrid MPI/OpenMP parallelisation. Comput. Fluids 179, 123–136. http://dx.doi.org/10.1016/j.compfluid.2018.10.013.

Ouro, P., Harrold, M., Ramirez, L., Stoesser, T., 2019b. Prediction of the wake behind a horizontal axis tidal turbine using a LES-ALM. In: Prog. CFD Wind Tidal Offshore Turbines. Springer, pp. 25–35. http://dx.doi.org/10.1007/978-3-030-11887-7_3, Chapter 4.

Ouro, P., Harrold, M., Stoesser, T., Bromley, P., 2017. Hydrodynamic loadings on a horizontal axis tidal turbine prototype. J. Fluids Struct. 71, 78–95. http://dx.doi.org/10.1016/j.jfluidstructs.2017.03.009.

Ouro, P., Stoesser, T., 2017. An immersed boundary-based large-eddy simulation approach to predict the performance of vertical axis tidal turbines. Comput. Fluids 152, 74–87. http://dx.doi.org/10.1016/j.compfluid.2017.04.003.

Ouro, P., Stoesser, T., 2019. Impact of environmental turbulence on the performance and loadings of a tidal stream turbine. Flow, Turbul. Combust. 102, 613–639. http://dx.doi.org/10.1007/s10494-018-9975-6.

Ouro, P., Stoesser, T., Fraga, B., Lopez-Novoa, U., 2018. Hydro3D, http://dx.doi.org/10.5281/zenodo.1200187.

Porté-Agel, F., Wu, Y.T., Chen, C.H., 2013. A numerical study of the effects ofwind direction on turbine wakes and power losses in a large wind farm. Energies 6 (10), 5297–5313. http://dx.doi.org/10.3390/en6105297.

Ramos, V., Carballo, R., Sanchez, M., Veigas, M., Iglesias, G., 2014. Tidal stream energy impacts on estuarine circulation. Energy Convers. Manag. 80, 137–149. http://dx.doi.org/10.1016/j.enconman.2014.01.027.

Sanz Rodrigo, J., Chávez Arroyo, R.A., Moriarty, P., Churchfield, M., Kosović, B., Réthoré, P.E., Hansen, K.S., Hahmann, A., Mirocha, J.D., Rife, D., 2017. Mesoscale to microscale wind farm flow modeling and evaluation. Wiley Interdiscip. Rev. Energy Environ. 6 (2), 1–30. http://dx.doi.org/10.1002/wene.214.

Shen, W.Z., Sørensen, J.N., Mikkelsen, R., 2005. Tip loss correction for actuator/navier–stokes computations. J. Sol. Energy Eng. 127 (2), 209–213. http://dx.doi.org/10.1115/1.1850488.

Shives, M., Crawford, C., 2016. Adapted two-equation turbulence closures for actuator disk RANS simulations of wind & tidal turbine wakes. Renew. Energy 92, 273–292. http://dx.doi.org/10.1016/j.renene.2016.02.026.

Sørensen, J.N., Mikkelsen, R.F., Dan, S., Ivanell, S., Sarmast, S., Andersen, S.J., 2015. Simulation of wind turbine wakes using the actuator line technique. Philos. Trans. A. Math. Phys. Eng. Sci. (373), 20140071. http://dx.doi.org/10.1098/rsta.2014.0071.

Stallard, T., Collings, R., Feng, T., Whelan, J., 2013. Interactions between tidal turbine wakes: experimental study of a group of three-bladed rotors.. Philos. Trans. A. Math. Phys. Eng. Sci. 371, 20120159. http://dx.doi.org/10.1098/rsta.2012.0159.

Stallard, T., Feng, T., Stansby, P.K., 2015. Experimental study of the mean wake of a tidal stream rotor in a shallow turbulent flow. J. Fluids Struct. 54, 235–246. http://dx.doi.org/10.1016/j.jfluidstructs.2014.10.017.

Stoesser, T., 2010. Physically realistic roughness closure scheme to simulate turbulent channel flow over rough beds within the framework of LES. J. Hydraul. Eng. 136 (10), 812–819. http://dx.doi.org/10.1061/(ASCE)HY.1943-7900.0000236.

Stoesser, T., 2014. Large-eddy simulation in hydraulics: Quo Vadis?. J. Hydraul. Res. 52 (4), 441–452. http://dx.doi.org/10.1080/00221686.2014.944227.

Uhlmann, M., 2005. An immersed boundary method with direct forcing for the simulation of particulate flows. J. Comput. Phys. 209 (2), 448–476. http://dx.doi.org/10.1016/j.jcp.2005.03.017.

Vennell, R., Funke, S.W., Draper, S., Stevens, C., Divett, T., 2015. Designing large arrays of tidal turbines: A synthesis and review. Renew. Sustain. Energy Rev. 41, 454–472. http://dx.doi.org/10.1016/j.rser.2014.08.022.

Whelan, J.I., Graham, J.M.R., Peiró, J., 2009. A free-surface and blockage correction for tidal turbines. J. Fluid Mech. 624, 281. http://dx.doi.org/10.1017/S0022112009005916.

Yang, X., Howard, K.B., Guala, M., Sotiropoulos, F., 2015a. Effects of a three-dimensional hill on the wake characteristics of a model wind turbine. Phys. Fluids 27 (2), 025103. http://dx.doi.org/10.1063/1.4907685.

Yang, X., Sotiropoulos, F., Conzemius, R.J., Wachtler, J.N., Strong, M.B., 2015b. Large-eddy simulation of turbulent flow past wind turbines/farms: the Virtual Wind Simulator (VWiS). Wind Energy 18 (12), 2025–2045. http://dx.doi.org/10.1002/we.1802.

Yang, X., Zhang, X., Li, Z., He, G., 2009. A smoothing technique for discrete delta functions with application to immersed boundary method in moving boundary simulations. J. Comput. Phys. 228 (20), 7821–7836. http://dx.doi.org/10.1016/j.jcp.2009.07.023.